RSC Sustainability

ROYAL SOCIETY OF CHEMISTRY

PAPER

View Article Online
View Journal | View Issue

Check for updates

Cite this: *RSC Sustainability*, 2025, **3**, 1550

Fuel production capacity and DFT analysis of cation modified perovskites for enhanced thermochemical CO_2 dissociation

Jian Cong,[abc] Eric Beche[a] and Stéphane Abanades[*a]

Solar thermochemical redox splitting of CO_2 using perovskite oxygen carriers in two-step cycles is a promising method for sustainable fuel production. In this study, a series of 23 potential perovskite candidates for CO production are designed, synthesized, and tested under the same experimental conditions. The material stability and the lattice structure are validated using Goldschmidt's tolerance factor and powder X-ray diffraction. For the reduction step, the high proportion of divalent cations ($Sr^{2+}/Ba^{2+}/Ca^{2+}$) in the A site promotes oxygen transfer, and the maximum oxygen yield reaches 386 μmol g^{-1} ($\delta = 0.164$) for $Gd_{0.6}Ca_{0.4}MnO_3$. DFT calculation results indicate that the multi-cationic doping in $La_{0.5}Sr_{0.2}Ba_{0.15}Ca_{0.15}MnO_3$ shows a smaller energy barrier for oxygen transfer compared with the single A-site doping in $La_{0.5}Sr_{0.5}MnO_3$, with an oxygen vacancy formation energy of 2.91 eV per (O atom), and it offers the most favorable CO yields of 225 and 227 μmol g^{-1} in two consecutive cycles. The designed $La_{0.25}Gd_{0.25}Sr_{0.25}Ca_{0.25}MnO_3$ further decreases the oxygen vacancy formation energy to 2.57 eV per (O atom). Based on the reaction rate analysis, the presence of B-site doping cations, such as in $La_{0.6}Sr_{0.4}Mn_{0.75}Zr_{0.25}O_3$ and $La_{0.5}Sr_{0.5}Mn_{0.8}Ce_{0.2}O_3$, increases the maximum oxidation rate, and the A-site multi doping of perovskites allows maintaining high CO production rates during the oxidation process. This work leverages tunable perovskite redox properties for enhanced CO production performance through DFT and thermochemical performance analysis, providing feasible guidance to promote CO_2 splitting by an active cation doping strategy.

Received 8th November 2024
Accepted 6th February 2025

DOI: 10.1039/d4su00698d

rsc.li/rscsus

Sustainability spotlight

New sustainable and alternative energy carriers are required to limit CO_2 emissions and climate change resulting from the intensive use of fossil fuels and their combustion. This study addresses the sustainable production of solar fuels from two-step CO_2 splitting cycles using solid oxide intermediates. This thermochemical pathway offers a thermodynamically favourable route for solar energy harvesting and decarbonized fuel production, as it converts the entire solar spectrum to supply the required high-temperature process heat, without using expensive catalysts or intermediate electricity production. Solar recycling/conversion of captured CO_2 to synthetic fuels is also an alternative to underground CO_2 sequestration. Accordingly, this can contribute to achieving the global net zero carbon emissions and sustainable development goals (particularly SDGs 7, 12 & 13).

1 Introduction

The direct conversion of solar energy into fuels by thermochemical methods achieves the utilization of the full solar spectrum, with no greenhouse gas generation and high energy storability in the form of solar chemical fuels.[1] Among the most attractive solar fuel production methods, the two-step redox cycles for splitting CO_2 or H_2O have been widely studied recently with relatively moderate reaction temperatures and high theoretical solar-to-fuel production efficiency up to 68%.[2,3] Temperatures typically in the range of 1400–1500 °C for the reduction step and experimental solar-to-fuel efficiencies in the range of 4–10% were achieved.[4–7] First, the metal oxides (MO_x) are reduced to the oxygen deficient state ($MO_{x-\delta}$) using concentrated solar energy as the process heat source. Then, the reduced oxides absorb the oxygen from CO_2 or H_2O at a relatively lower oxidation temperature. The redox reactions are presented below:[8,9]

$$MO_x \rightarrow MO_{x-\delta} + \frac{\delta}{2}O_2 \tag{1}$$

$$MO_{x-\delta} + \delta H_2O/CO_2 \rightarrow MO_x + \delta CO/H_2 \tag{2}$$

Ceria (CeO_2) and perovskite-based oxides (ABO_3 type) are promising oxygen carriers for thermochemical redox reactions.[10,11] The rapid fuel production kinetics and multi-cycle stability of ceria make it an attractive option in the past

---

[a] *CNRS, Processes, Materials and Solar Energy Laboratory (PROMES), 7 rue du Four Solaire, 66120 Odeillo Font-Romeu, France. E-mail: stephane.abanades@promes.cnrs.fr*

[b] *Institute of Electrical Engineering, Chinese Academy of Sciences, Beijing, 100190, China*

[c] *University of Chinese Academy of Sciences, Beijing, 100049, China*

several years.[12] However, the low capacity for oxygen non-stoichiometry of reduced ceria limits the maximum fuel production yield.[13] To improve the fuel production potential of redox materials, ABO_3 type perovskites have been widely studied recently because of their strong oxygen transfer capacity and the large number of available formulations.[14,15] Typically, $LaMnO_3$-based perovskites present excellent fuel production performance with an effective cation doping.[16–24] Nair *et al.* found that $La_{0.5}Sr_{0.5}MnO_3$ perovskite synthesized by the Pechini method yielded an optimum CO production and Sr^{2+} was the best A-site cation dopant.[25] Subsequent studies investigated the CO production of Ba/Sr/Co/Fe/Ni/Ce substituted $LaMnO_3$ perovskites, and the results proved that $La_xSr_{1-x}MnO_3$ provided excellent fuel production capacity, while $La_{0.6}Sr_{0.4}(Ce_yMn_{1-y})O_3$ showed enhanced CO_2 splitting performance.[26,27] Through thermodynamic analysis, Carrillo *et al.* reported that $La_{0.6}Sr_{0.4}CrO_{3-\delta}$ has a lower CO_2 splitting Gibbs free energy compared with $La_{0.6}Sr_{0.4}MnO_{3-\delta}$, and the synthesized $La_{0.6}Sr_{0.4}Cr_{0.85}Mn_{0.15}O_3$ showed a fast CO production rate of 1.5 mL min^{-1} g^{-1}.[20] Experimentally, the promising perovskites such as $CeTi_2O_6$, $La_{0.6}Sr_{0.4}Mn_{0.6}Al_{0.4}O_3$ and $BaMn_{0.75}Ce_{0.25}O_3$ with B site substitution of Mn by Al or Ce showed a rapid oxidation kinetic rate and displayed large reaction entropies.[28–32] Although previous studies have proposed numerous high-performance perovskites, the different experimental operation conditions make it difficult to compare the fuel production results.[33] In this context, we performed the thermogravimetry analyses of 23 potential perovskites for comparison of their redox activity in the context of two-step CO_2 splitting. This is one of the first studies that analyze the fuel production performance of a large number of potential perovskites with different doping strategies under the same experimental conditions. The materials were synthesized by the Pechini sol–gel method and characterized by X-ray diffraction.

The perovskite's oxygen transfer capacity determines the maximum fuel yield and the reaction kinetic rate limits the solar-to-fuel conversion efficiency. Normally, perovskites with excellent oxygen transfer capacity show a high reduction extent (oxygen release), but at the expense of a thermodynamic limitation during oxidation, thus requiring a large temperature swing between redox steps or large oxidant excess to overcome the thermodynamic barrier. The oxidation step can further be hindered by a low kinetic rate due to limitations of the solid–gas surface reaction, thereby limiting the rate of fuel production.[28] The oxidation is an exothermic reaction. Thermodynamically, a low reaction temperature is beneficial for H_2O or CO_2 splitting. However, the kinetic rate decreases at low reaction temperatures. Thus, both thermodynamic and kinetic limitations occur in the oxidation process. The fuel production kinetics in the oxidation process is important because rapid fuel production is needed to decrease the required energy input and increase the fuel production efficiency. To improve the fuel production performance, perovskites with single-cation doping, double-cation doping (cations doped in both A and B sites), and multi-cation doping (more than two cations doped in the A or B site) were synthesized in this work. Actually, some A-site high doping perovskites have been studied with excellent CO production performance.[34,35] Therefore, several potential multi-cation doped perovskites were considered to compare the CO yields with single/double cation doped perovskites. We chose the lanthanide elements La, Gd, and Sm as the A-site base elements, and Mn as the B-site base element. As shown in Fig. 1, the divalent cations Sr^{2+}, Ba^{2+} and Ca^{2+} are doped in the A site to promote oxygen transfer, and the high valence cations Zr^{4+}, Cr^{3+}, Fe^{3+}, Al^{3+} and Ce^{3+} are doped in the B site to adjust the reaction kinetic rate during oxidation. The selected perovskites were synthesized primarily because these formulations were not considered before. For the A site cation doping, the divalent cations (Sr^{2+}, Ba^{2+}, and Ca^{2+}) and the lanthanide elements (Gd^{3+} and Sm^{3+}) were used to substitute La^{3+} for better oxygen transfer capacity. Substituting divalent Ca^{2+}, Sr^{2+}, and Ba^{2+} cations for La^{3+}, Pr^{3+}, Sm^{3+} or Gd^{3+} (A site)

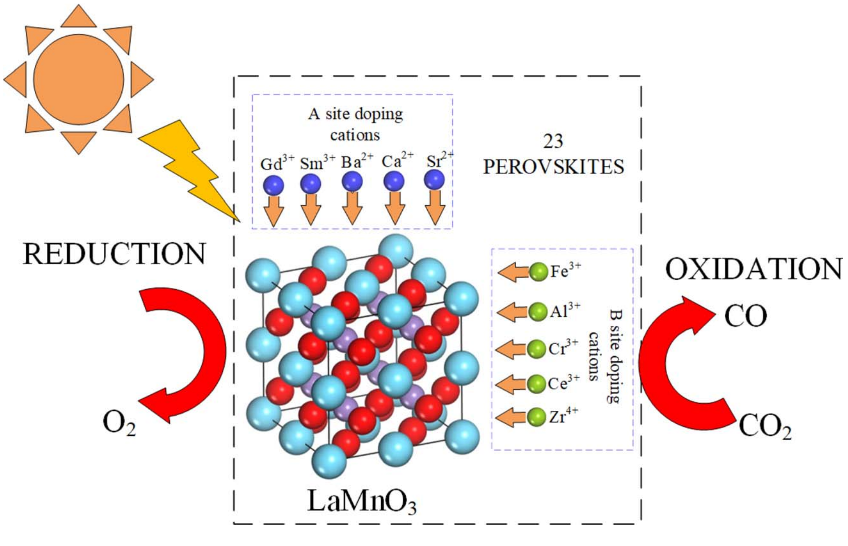

Fig. 1 Schematic diagram of tunable CO production of perovskites by doping cations.

aims to create several effects leading to structural changes/deviations, cation deficiency, oxygen non-stoichiometry, improved catalytic oxidation activity, and controlled transition between Mn^{3+} and Mn^{4+}. The substitution of divalent cations causes the valence of the Mn ion to increase above 3, which favors the cation reduction from a high valence state to Mn^{3+}. Similarly, B-site substitution has also beneficial effects. Experimentally, previous studies suggested that B-site cation doping (Al^{3+}, Zr^{4+}, Ce^{3+}, Fe^{3+}, and Cr^{3+}) of $LaMnO_3$ perovskites led to rapid oxidation kinetic rates. Basically, cationic doping of perovskites in the A or B site was shown to be beneficial for the generation of oxygen vacancies within the perovskites. For multi-doped perovskites, the increment of the element number can increase the molar configurational entropy of the perovskites ($S_{\text{config}} = -R\cdot\sum_{i=1}^{N} x_i \ln x_i$, where R is the universal gas constant and x_i is the molar fraction of the element i).[36] The high entropy value makes the oxidation process easier to occur because of the low value of reaction Gibbs free energy. The material stability is predicted using the calculated Goldschmidt's tolerance factor and further validated using X-ray diffraction analysis results. Through the thermogravimetric analyses, the CO yields of perovskites are determined and the first principles DFT study of oxygen vacancy formation energy demonstrates the beneficial effects of multi-cation doping on oxygen transfer. Apart from the CO yields, the evolved gas production rates of synthesized perovskites are also obtained in this work. The study analyzes the experimental production performance of the 23 potential perovskites in terms of fuel yields and gas production rates, which supports the search for novel high-performance perovskites for thermochemical CO_2 splitting.

2 Materials and methods

2.1 Materials synthesis

The doped perovskites were synthesized by the Pechini sol–gel method.[37] The main raw salt precursors were supplied by the Alfa Aesar company, which include $Gd(NO_3)_3\cdot 6H_2O$ (99.9%), $La(NO_3)_3\cdot 6H_2O$ (99.9%), $Sm(NO_3)_3\cdot 6H_2O$ (99.9%), $Sr(NO_3)_2$ (99%), $Ca(NO_3)_2\cdot 4H_2O$ (98%), $Mn(NO_3)\cdot 4H_2O$ (97.5%), $Fe(NO)_3\cdot 9H_2O$ (98%), $Al(NO_3)_3\cdot 9H_2O$ (99%), $Ce(NO_3)_3\cdot 6H_2O$ (99%), $ZrN_2O_7\cdot 6H_2O$ (99.5%), $Cr(NO_3)_3\cdot 6H_2O$ (99%), citric acid $C_6H_8O_7$ (99.5%) and ethylene glycol $C_2H_6O_2$ (99%). First, the nitrates were added into the beaker based on the designed molar proportion. Then, citric acid was mixed with the nitrates in a molar ratio of 2 : 1, dissolving in deionized water. After the nitrate solution was stirred and heated to 70 °C, glycol was added to the solution. Then, the solution heating continued to 85 °C with stirring at this temperature to form the gel. The formed gel was placed into a drying oven at 120 °C for 3 h. A two-step calcination process was performed to avoid the loss of Mn.[38] First, the powders were calcined at 800 °C for 90 min followed by cooling to room temperature. Then, the powders were heated to 1400 °C for 6 h (3 h ramp up and 3 h dwell) and cooled to form a stable powder structure.

2.2 Experimental methods

To determine the crystal structures and the lattice parameters of the synthesized perovskite powders, the powder X-ray diffraction (PXRD) patterns were obtained at room temperature with an X'Pert Pro PANalytical diffractometer with Cu Kα radiation ($\lambda = 0.15418$ nm). The diffraction angles (2θ) were measured in the range of 10–90° with a step size of 0.017°. The crystal and lattice parameters were analyzed by cell refinement using Jade 6.0 software.

The gas production yields and redox performance of the synthesized perovskites in the two-step thermochemical redox reactions were obtained by thermogravimetry analysis (TGA) using a thermal analyzer SETARAM Setsys Evolution. The processed powders with a weight of about 100 mg were placed in a platinum crucible. The reduction temperature was set at 1400 °C with a heating rate of 20 K min^{-1}. After holding the samples at 1400 °C for 45 min, the reduced perovskites were cooled to the oxidation temperature of 1050 °C, holding for 1 h. In the reduction step, high purity argon (99.999% purity, 2 ppm O_2) was used with a flow rate of 20 N mL min^{-1} (normal conditions). During the oxidation step, CO_2 (with 99.995% purity) was injected at a flow rate of 10 N mL min^{-1} with a CO_2 molar fraction of 50% in argon. Two consecutive cycles were carried out to provide an overview of the material's redox performance and capacity for CO_2 splitting, and a comparison among the considered formulations in terms of fuel yields and gas production rates. The main aim of this work was to unravel the effect of cation modified perovskites on performance in the fuel production process, which helps for the further selection of effective cations for CO_2 splitting. Therefore, various cations incorporated into perovskites were tested under the same experimental conditions. For subsequent cycles after the second cycle, it is generally admitted that the fuel production capacity does not evolve significantly compared to the initial two cycles because the morphological and structural changes generally occur in the first cycle. Thus, the performance of the second cycle is representative of the material's redox activity.

The sample mass variations (loss during reduction due to O_2 release and gain during oxidation due to O atom replenishment from CO_2 gas to produce CO) were measured continuously to determine the O_2 and CO production yields (*i.e.*, the amounts produced per unit mass of perovskite).[39]

The oxygen yield (mol g^{-1}) can be obtained using eqn (3):[37]

$$Y_{O_2} = \frac{\Delta m}{2M_O m_{\text{ini}}} \tag{3}$$

where Δm is the perovskite's mass change during the reduction process (g), M_O is the molar mass of the atomic oxygen (16 g mol^{-1}), and m_{ini} is the initial mass of the perovskites (*g*).

To determine the reduction extent, the oxygen non-stoichiometry (δ) is calculated using eqn (4):

$$\delta = \frac{\Delta m}{m_{\text{ini}}}\cdot\frac{M_P}{M_O} \tag{4}$$

where M_P is the molar mass of the perovskites. The CO yields during oxidation are calculated using the following equation:

$$Y_{\mathrm{CO}} = \frac{\Delta m}{M_{\mathrm{O}} m_{\mathrm{ini}}} \tag{5}$$

In the redox reactions, the O_2 and CO production rates (mol g^{-1} s^{-1}) can be calculated using the following equations:

$$r_{\mathrm{O_2}} = \frac{r_{\mathrm{m}}}{2 \cdot M_{\mathrm{O}} \cdot m_{\mathrm{ini}}} \tag{6}$$

$$r_{\mathrm{CO}} = \frac{r_{\mathrm{m}}}{M_{\mathrm{O}} \cdot m_{\mathrm{ini}}} \tag{7}$$

where r_{m} (g s^{-1}) is the rate of sample mass variation obtained from the first order derivative of the mass change.

3 Results and discussion

3.1 Materials characterization

The stability of ABO_3 type perovskite structures can be predicted using Goldschmidt's tolerance factor, which reflects the relationship between the average A–O and B–O distances. For the ideal cubic perovskite structure, the tolerance value (t) is 1. The perovskite phase will be distorted to a tetrahedral or hexagonal phase when $t > 1$, and orthorhombic or rhombohedral phases will form when $t < 0.9$.[40] The original equation is presented below :[41,42]

$$t = \frac{r_{\mathrm{A}} + r_{\mathrm{O}}}{\sqrt{2}(r_{\mathrm{B}} + r_{\mathrm{O}})} \tag{8}$$

where r_{A}, r_{B} and r_{O} are the ionic radii of cations A, B and O, respectively. The ionic radii of cations are obtained from Shannon.[43] For the ABO_3 type perovskites, the 12-fold coordinated A site is filled with low valence metal cations and the 6-fold coordinated B site is occupied by the high valence metal cations. When the A or B site is doped with more than one cation, we adopt the equivalent ionic radius method to get the average cation radii of the A and B site elements.[44,45]

$$r_{\mathrm{X}} = \sum \lambda_i r_i \quad (\mathrm{X} = \mathrm{A}, \mathrm{B}) \tag{9}$$

Table 1 Tolerance factors and XRD refinement parameters of perovskites

	Goldschmidt tolerance factor	Lattice parameters			Crystallite size (nm)
		a (Å)	b (Å)	c (Å)	
Single A-site cation doping					
$GdMnO_3$	0.897	5.324	5.792	7.468	86.3
$Gd_{0.75}La_{0.25}MnO_3$-Before	0.92	5.376	5.738	7.535	66.1
$Gd_{0.75}La_{0.25}MnO_3$-After		5.384	5.813	7.526	65.1
$Gd_{0.9}Ca_{0.1}MnO_3$-B	0.905	5.383	5.830	7.519	63.1
$Gd_{0.9}Ca_{0.1}MnO_3$-A		5.375	5.832	7.522	63.6
$Gd_{0.75}Ca_{0.25}MnO_3$-B	0.918	5.498	5.890	7.536	39.3
$Gd_{0.75}Ca_{0.25}MnO_3$-A		5.510	5.913	7.569	31.1
$Gd_{0.6}Ca_{0.4}MnO_3$-B	0.93	5.458	5.860	7.481	38.4
$Gd_{0.6}Ca_{0.4}MnO_3$-A		5.485	5.874	7.558	26.5
$Gd_{0.75}Sr_{0.25}MnO_3$-B	0.927	5.431	5.828	7.430	44.2
$Gd_{0.75}Sr_{0.25}MnO_3$-A		5.442	5.843	7.449	41.6
Multiple cation doping					
$Gd_{0.75}Ca_{0.25}Mn_{0.75}Fe_{0.25}O_3$	0.92	5.449	5.846	7.482	34.5
$Gd_{0.6}Ca_{0.4}Mn_{0.75}Cr_{0.25}O_3$-B	0.838	5.418	5.818	7.430	48
$Gd_{0.6}Ca_{0.4}Mn_{0.75}Cr_{0.25}O_3$-A		5.444	5.845	7.467	42.3
$La_{0.6}Sr_{0.4}Mn_{0.5}Fe_{0.25}Al_{0.25}O_3$-B	0.948	3.875	3.875	3.875	47.9
$La_{0.6}Sr_{0.4}Mn_{0.5}Fe_{0.25}Al_{0.25}O_3$-A		3.881	3.881	3.881	64.5
$La_{0.6}Sr_{0.4}Mn_{0.75}Ce_{0.25}O_3$-B	1.009	3.869	3.869	3.869	40.8
$La_{0.6}Sr_{0.4}Mn_{0.75}Ce_{0.25}O_3$-A		3.871	3.871	3.871	35.6
$La_{0.6}Sr_{0.4}Mn_{0.75}Zr_{0.25}O_3$-B	0.982	3.901	3.901	3.901	36.5
$La_{0.6}Sr_{0.4}Mn_{0.75}Zr_{0.25}O_3$-A		3.904	3.904	3.904	25.5
$La_{0.3}Gd_{0.3}Sr_{0.4}MnO_3$-B	0.954	3.908	3.908	3.908	52.2
$La_{0.3}Gd_{0.3}Sr_{0.4}MnO_3$-A		3.893	3.893	3.893	65.1
$La_{0.25}Gd_{0.25}Sr_{0.25}Ca_{0.25}MnO_3$-B	0.955	3.908	3.908	3.908	37.9
$La_{0.25}Gd_{0.25}Sr_{0.25}Ca_{0.25}MnO_3$-A		3.880	3.880	3.880	50.6
$Sm_{0.5}Sr_{0.5}Mn_{0.8}Ce_{0.2}O_3$-B	0.94	5.417	7.641	5.446	36.6
$Sm_{0.5}Sr_{0.5}Mn_{0.8}Ce_{0.2}O_3$-A		5.419	7.714	5.441	52.9
$La_{0.5}Sr_{0.5}Mn_{0.8}Ce_{0.2}O_3$-B	0.96	5.461	5.461	5.461	38.87
$La_{0.5}Sr_{0.5}Mn_{0.8}Ce_{0.2}O_3$-A		5.468	5.468	5.468	41.4
$La_{0.5}Sr_{0.2}Ba_{0.15}Ca_{0.15}MnO_3$-B	1	3.869	3.869	3.869	26.8
$La_{0.5}Sr_{0.2}Ba_{0.15}Ca_{0.15}MnO_3$-A		3.875	3.875	3.875	35.4
$La_{0.5}Sr_{0.2}Ba_{0.15}Ca_{0.15}Mn_{0.7}Ce_{0.15}Zr_{0.15}O_3$-B	0.964	3.876	3.876	3.876	33.8
$La_{0.5}Sr_{0.2}Ba_{0.15}Ca_{0.15}Mn_{0.7}Ce_{0.15}Zr_{0.15}O_3$-A		3.884	3.884	3.884	27.88
$Y_{1/6}La_{1/6}Sm_{1/6}Sr_{1/6}Ba_{1/6}Ca_{1/6}Mn_{0.7}Ce_{0.15}Al_{0.15}O_3$-B	0.956	5.505	5.505	5.505	45.8
$Y_{1/6}La_{1/6}Sm_{1/6}Sr_{1/6}Ba_{1/6}Ca_{1/6}Mn_{0.7}Ce_{0.15}Al_{0.15}O_3$-A		5.477	5.477	5.477	66.6

where λ_i is the molar proportion of the element i and r_i represents the ionic radius of i. For example, the tolerance factor of $La_{0.6}Sr_{0.4}Mn_{0.5}Fe_{0.25}Al_{0.25}O_3$ is calculated using eqn (10).

$$t = \frac{0.6r_{\mathrm{La}} + 0.4r_{\mathrm{Sr}} + r_{\mathrm{O}}}{\sqrt{2}(0.5r_{\mathrm{Mn}} + 0.25r_{\mathrm{Fe}} + 0.25r_{\mathrm{Al}} + r_{\mathrm{O}})} \tag{10}$$

The tolerance factor calculation results of the target perovskites are shown in Table 1, ranging from 0.838 to 1.009. The results from a previous study show that perovskites can remain in stable phases in the t range of $0.813 < t < 1.107$.[46] Therefore, all of the designed materials are predicted to form stable perovskite structures, which are consistent with the X-ray diffraction results in Table 1. The $GdMnO_3$ and $SmMnO_3$ based perovskites present an orthorhombic structure, and the $LaMnO_3$ based perovskites present a cubic structure. Goldschmidt's tolerance factor is useful in preliminary design and can help to assess the perovskite's stability, supporting the effective synthesis and experimental performance studies of the designed materials.

The crystallite sizes and lattice parameters are presented in Table 1. Crystallite sizes of synthesized perovskites are calculated using the Scherrer equation:[47]

$$D = \frac{K \cdot \lambda}{\beta \cdot \cos\theta} \tag{11}$$

where D is the mean crystallite size (nm), β is the full width at half maximum (FWHM) intensity, λ is the X-ray wavelength, θ is the Bragg angle, and K is a dimensionless shape factor, which is assumed to be 0.89.

Fig. 2 shows the change of the crystallite sizes before (black symbols) and after (red symbols) the cycling experiments. For most of the single and double cation doped perovskites, the crystallite sizes decrease after the reaction, indicating that the materials are not significantly sintered after the experiment. In contrast, the multi-cation doped perovskites show an obvious increment in the crystallite size.

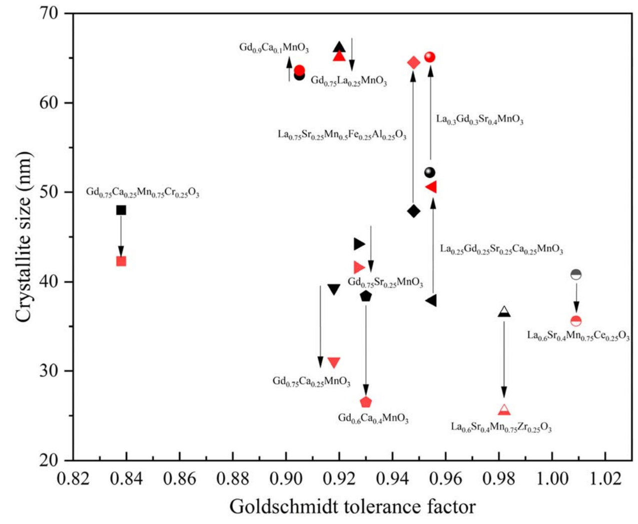

Fig. 2 Crystallite sizes and Goldschmidt tolerance factors of perovskites.

The X-ray diffraction patterns of fresh and cycled materials are presented in Fig. 3. The synthesized perovskites are fitted with the related ICSD (inorganic crystal structure database) patterns. For the single cation doped materials, the replacement of Gd^{3+} (1.107 Å) with the larger ionic radius elements Ca^{2+} (1.34 Å), La^{3+} (1.36 Å), and Sr^{2+} (1.44 Å) causes the shift of the main Bragg peak (112) to lower angles, indicating that the cations are successfully incorporated into the parent perovskite. Fig. 3(b) shows that the high Ce^{4+} and Zr^{4+} doping proportions have generated side peaks of $SrZrO_3$ and CeO_2. The same situation occurs in $Gd_{0.75}Ca_{0.25}Mn_{0.75}Fe_{0.25}O_3$, which is extremely sintered after the reaction. It is noted that cation doping in the B site may decrease the purity of target perovskites and generate byproducts. All of the multiple A site doped perovskites remain in the form of pure phases after the experiments, revealing that cation doping in the A site does not affect the material's phase purity.

3.2 Thermochemical reaction performance

A summary of the obtained thermochemical reaction yields of synthesized perovskites is presented in Table 2. The overall fuel production performance with O_2/CO yields and conversion ratios are reported. The results help to assess the material's reduction capacity and the CO production performance in two successive cycles, and the CO/O_2 conversion ratio is determined based on the experimental results.

3.2.1 Reduction capacity. The synthesized perovskites need to produce sufficient oxygen vacancies to increase maximum CO yields during oxidation. As shown in Fig. 4, TGA of materials was used to determine the mass variation of (a) single doping, (b) double doping, and (c) multiple cation doping of perovskites during two successive reduction–reoxidation cycles. The mass loss in the first reduction step represents the oxygen transfer capacity. Overall, the perovskites $Gd_{0.6}Ca_{0.4}MnO_3$, $Sm_{0.5}Sr_{0.5}MnO_3$ and $La_{0.25}Gd_{0.25}Sr_{0.25}Ca_{0.25}MnO_3$ exhibit the largest mass loss, reaching 1.2%, whereas $Gd_{0.75}La_{0.25}MnO_3$ shows the lowest reduction extent, with a mass loss of only 0.23%. These results reveal that doping of divalent cations in the A site (Sr^{2+}, Ca^{2+}, and Ba^{2+}) is beneficial for the generation of oxygen vacancies within the perovskites. Besides, the trivalent cations in the A site also influence the oxygen transfer, with the reduction capacity from strong to weak being in the following order: $Gd^{3+} > Sm^{3+} > Pr^{3+} > La^{3+}$. Compared with the single doping of perovskites in Fig. 4(a), the mass losses during reduction of Cr^{3+}/Fe^{3+} doped $Gd_{0.75}Ca_{0.25}Mn_{0.75}Cr_{0.25}O_3$/$Gd_{0.75}Ca_{0.25}Mn_{0.75}Fe_{0.25}O_3$ and Ce^{3+} doped $Sm_{0.5}Sr_{0.5}Mn_{0.8}Ce_{0.2}O_3$/$La_{0.5}Sr_{0.5}Mn_{0.75}Ce_{0.25}O_3$ decrease with the existence of B site doping cations. For multi-cation doped perovskites, the mass loss of $La_{0.5}Sr_{0.2}Ba_{0.15}Ca_{0.15}MnO_3$ is 0.5% larger than that of $La_{0.5}Sr_{0.2}Ba_{0.15}Ca_{0.15}Mn_{0.7}Ce_{0.15}Zr_{0.15}O_3$. The above results indicate the unfavorable effect of B site doping cations on oxygen production. Overall, the presence of Gd^{3+} and the high doping proportion of divalent cations are beneficial for generating more oxygen in the reduction step.

Fig. 5 shows the oxygen yields of perovskites in two successive redox cycles by plotting both the oxygen yield and δ values

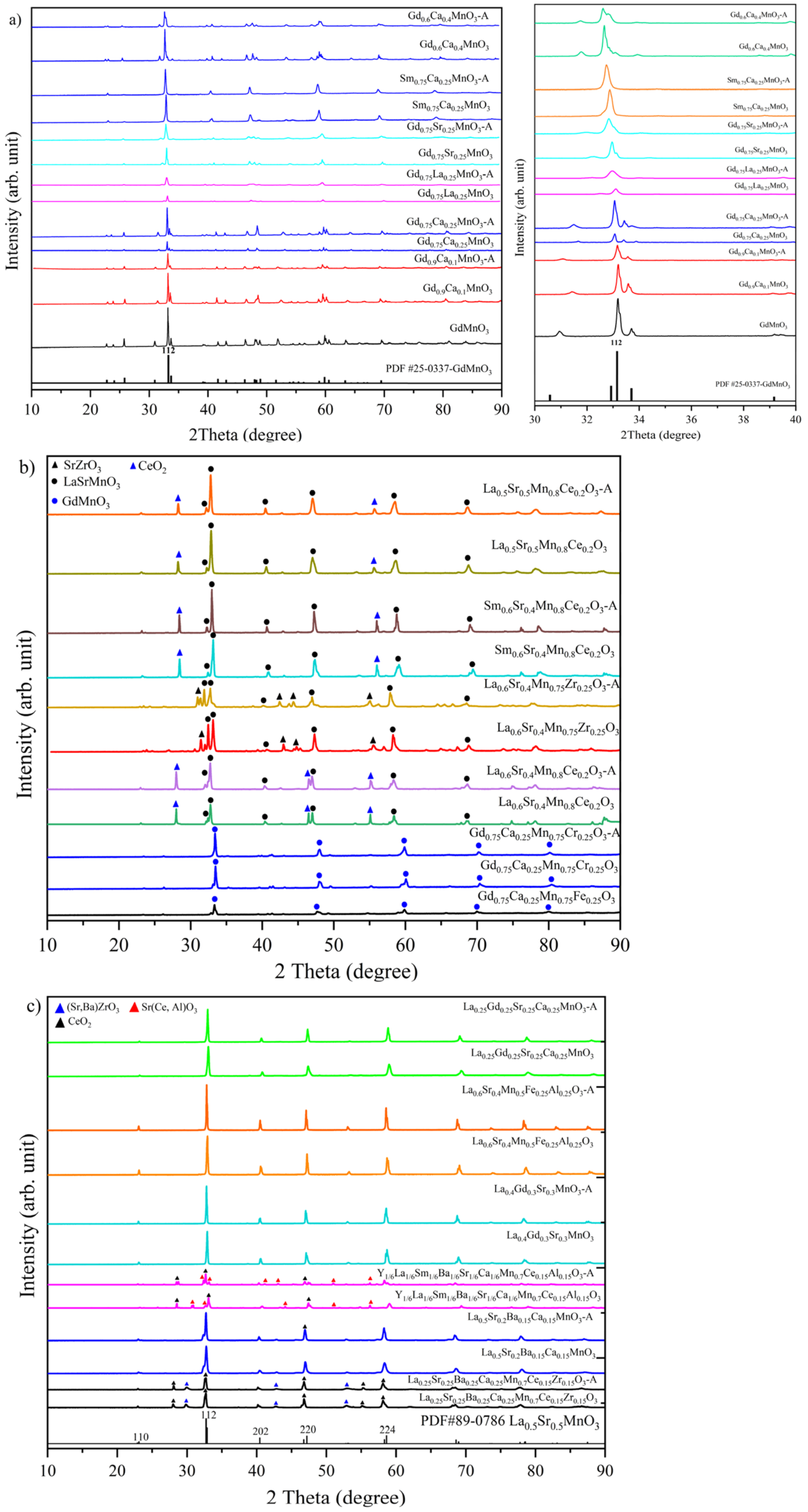

Fig. 3 X-ray powder diffraction patterns of perovskites: (a) single cation doping, (b) double cation doping, (c) multiple cation doping before and after the thermochemical cycles between 1050 °C and 1400 °C.

for each material to highlight the reduction capacity. Fig. 5(a and b) represent the oxygen production yields of perovskites in the first reduction step, and Fig. 5(c and d) show the oxygen production yields in the second reduction step. For the first reduction step, the maximum oxygen yield reaches 386 μmol g^{-1} ($\delta = 0.164$) from $Gd_{0.6}Ca_{0.4}MnO_3$, but the oxygen yield

Table 2 Thermochemical reaction yields of 23 perovskites in two consecutive cycles

	First cycle			Second cycle		
	O_2 (μmol g^{-1})	CO (μmol g^{-1})	$n(CO)/n(O_2)$	O_2 (μmol g^{-1})	CO (μmol g^{-1})	$n(CO)/n(O_2)$
$Gd_{0.75}La_{0.25}MnO_3$	78	24	0.31	22	25	1.13
$Gd_{0.75}Ca_{0.25}MnO_3$	191	144	0.75	104	152	1.46
$Gd_{0.75}Sr_{0.25}MnO_3$	285	158	0.554	97	166	1.71
$Gd_{0.75}Ca_{0.25}Mn_{0.75}Fe_{0.25}O_3$	307	119	0.387	92	136	1.48
$Gd_{0.75}Ca_{0.25}Mn_{0.75}Cr_{0.25}O_3$	318	108	0.339	99	109	1.1
$Gd_{0.9}Ca_{0.1}MnO_3$	100	59	0.59	48	63	1.3
$Gd_{0.6}Ca_{0.4}MnO_3$	386	145	0.375	113	156	1.38
$La_{0.6}Sr_{0.4}Mn_{0.5}Fe_{0.25}Al_{0.25}O_3$	257	230	0.894	121	211	1.74
$La_{0.25}Gd_{0.25}Sr_{0.25}Ca_{0.25}MnO_3$	368	184	0.5	105	190	1.81
$Sm_{0.75}Ca_{0.25}MnO_3$	140	112	0.8	73	128	1.75
$La_{0.6}Sr_{0.4}Mn_{0.75}Zr_{0.25}O_3$	112	92	0.821	52	98	1.88
$La_{0.6}Sr_{0.4}Mn_{0.75}Ce_{0.25}O_3$	126	178	1.412	95	178	1.87
$Pr_{0.5}Sr_{0.5}MnO_3$	268	153	0.57	90	160	1.77
$Sm_{0.5}Sr_{0.5}MnO_3$	373	168	0.45	101	175	1.73
$La_{0.5}Sr_{0.5}MnO_3$	232	190	0.82	104	195	1.87
$Sm_{0.6}Ca_{0.4}Mn_{0.8}Al_{0.2}O_3$	206	213	1.03	180	212	1.17
$Sm_{0.75}Sr_{0.25}MnO_3$	117	177	1.51	95	180	1.89
$La_{0.3}Gd_{0.3}Sr_{0.4}MnO_3$	225	182	0.8	103	183	1.77
$La_{0.5}Sr_{0.2}Ba_{0.15}Ca_{0.15}MnO_3$	271	225	0.83	113	227	2
$La_{0.5}Sr_{0.5}Mn_{0.8}Ce_{0.2}O_3$	205	205	1	110	204	1.85
$Sm_{0.5}Sr_{0.5}Mn_{0.8}Ce_{0.2}O_3$	292	164	0.56	97	169	1.74
$La_{0.5}Sr_{0.2}Ba_{0.15}Ca_{0.15}Mn_{0.7}Ce_{0.15}Zr_{0.15}O_3$	118	162	1.37	88	161	1.82
$Y_{1/6}La_{1/6}Sm_{1/6}Sr_{1/6}Ba_{1/6}Ca_{1/6}Mn_{0.7}Ce_{0.15}Al_{0.15}O_3$	319	127	0.39	91	143	1.57

decreases to 113 μmol g^{-1} in the second cycle. The main reason is that the reaction kinetic rate limits the oxygen vacancy generation in the second cycle. The maximum oxygen non-stoichiometry value of $Gd_{0.6}Ca_{0.4}MnO_3$ is over 10 times larger than the value of CeO_2 ($\delta = 0.016$).[48] An almost linear relationship can be obtained between the oxygen yield (μmol g^{-1}) and δ in Fig. 5. However, the amount of oxygen produced per unit mass of oxide also relies on the molecular weight of the material, which explains why the values are not directly proportional. $Sm_{0.6}Ca_{0.4}Mn_{0.8}Al_{0.2}O_3$ shows the largest oxygen yield at 180 μmol g^{-1} in the second reduction step, with a δ value of 0.07. The high ratio of Ca^{2+} incorporation leads to the best reduction performance in the successive cycles compared with other materials. The cation doping in the B site decreases the oxygen transfer capacity in the first cycle. However, doping of B site cations (Al^{3+}, Fe^{3+}, and Ce^{3+}) presents high oxygen yields in the second redox cycle. Owing to the refill of more oxygen vacancies in the first oxidation step, B-site doped perovskites have improved oxygen production capacity in the successive second reduction step.

For the A site multi-doping Mn-based perovskites, the reduction extent can be calculated by the variation in the Mn ion valence. As shown in Fig. 6, the decrease in Mn ion valence for $Gd_{0.6}Ca_{0.4}MnO_3$ is larger than that for other perovskites, reaching a value of 0.33. With the same initial Mn ion valence, the reduction capacity of high doping $La_{0.25}Gd_{0.25}Sr_{0.25}Ca_{0.25}MnO_3$ is better than that of $La_{0.5}Sr_{0.2}Ba_{0.15}Ca_{0.15}MnO_3$. For low cation doping proportions, the Sr^{2+} incorporation shows better reduction performance than the Ca^{2+} substituted $GdMnO_3$. It is observed that the Mn ion valence of single cation doped perovskites tends to reach a similar final value (below 3.1 in any case), whereas the A site high doping of perovskites cannot reach such a low Mn ion valence state.

With the same A-site doping proportion of divalent cations, $La_{0.5}Sr_{0.5}MnO_3$, $La_{0.5}Sr_{0.2}Ba_{0.15}Ca_{0.15}MnO_3$ and $La_{0.25}Gd_{0.25}Sr_{0.25}Ca_{0.25}MnO_3$ show different oxygen production capacities. The removal of oxygen from perovskites in the reduction process needs to overcome the energy barrier, which is noted as the oxygen vacancy formation energy ΔE_V (eV per (O atom)). In this work, the ΔE_V values were predicted using the Cambridge serial total energy package (CASTEP) of Material Studio software through the density functional theory (DFT) calculation, which is based on the periodic boundary conditions and plane-wave expansion of the wave function.[49,50] The calculation equation is presented below:[51]

$$\Delta E_V = E_{vac}(ABO_{3-\delta}) + \frac{1}{2}E_{O_2} - E(ABO_3) \qquad (12)$$

where E_{vac} and E are the DFT total energies of the cubic perovskite cells with and without an oxygen vacancy (eV), and E_{O2} is the energy of oxygen molecules (eV). The calculations are based on density functional theory with functions of generalized gradient approximation (GGA) and Perdew–Burke–Ernzerhof (PBE), using the ultrasoft pseudopotentials.[52,53] The supercells of 2 × 2 × 2 are established with 40 atoms, and 2 × 2 × 2 k point meshes are generated using the Monkhorst–Pack scheme. The setting parameters of analyses include: a cutoff energy of 650 eV, self-consistent field (SCF) of 1.0×10^{-8} eV per atom, maximum force of 0.01 eV per atom, maximum displacement of 5×10^{-4} Å and energy convergence criteria of 2.0×10^{-5} eV per

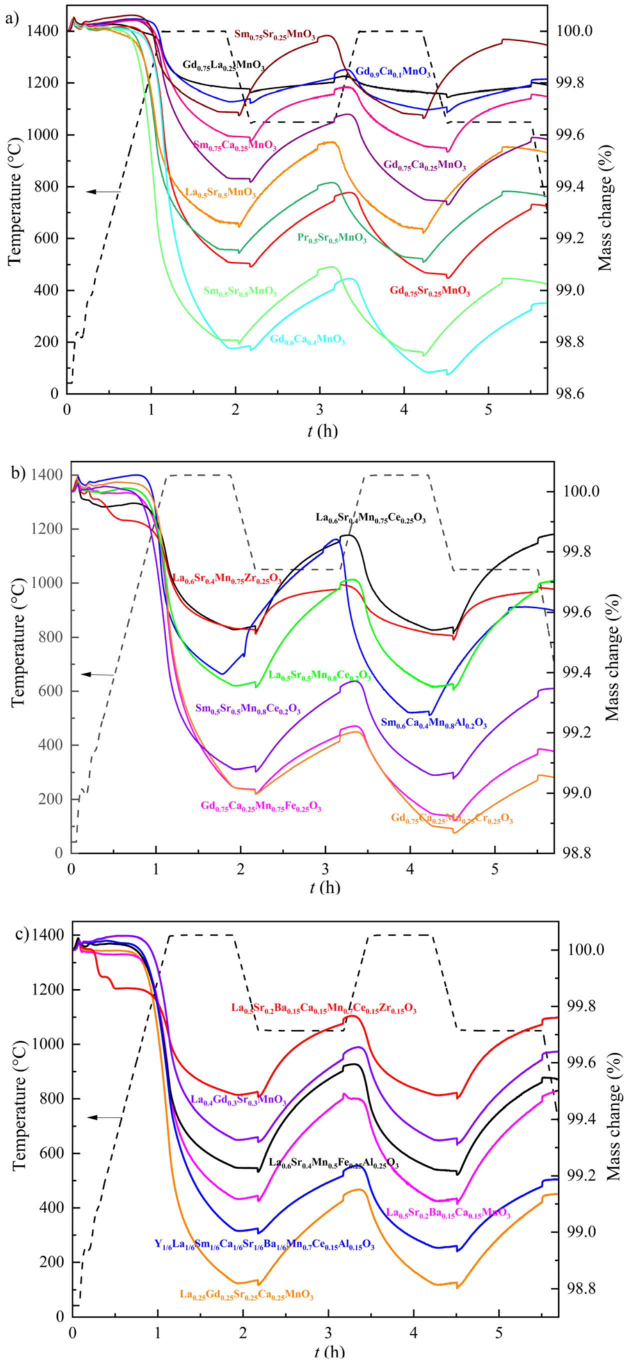

Fig. 4 TGA mass changes of (a) single doping, (b) double doping, and (c) multi-doping of perovskites during two successive thermochemical cycles between 1050 °C and 1400 °C.

atom. The calculation result of oxygen vacancy formation energy is first verified using existing $LaMnO_3$ data (3.927 eV per O atom), obtained by Emery *et al.*[14] The obtained value in our simulation is 3.897 eV per (O atom), with an energy difference of 0.03 eV per (O atom). Then, the divalent cation substitution of La^{3+} in the A site of the $LaMnO_3$ supercell in the model and the oxygen defected structure of supercells are presented in Fig. 7. It is often considered that the oxygen vacancy formation energy

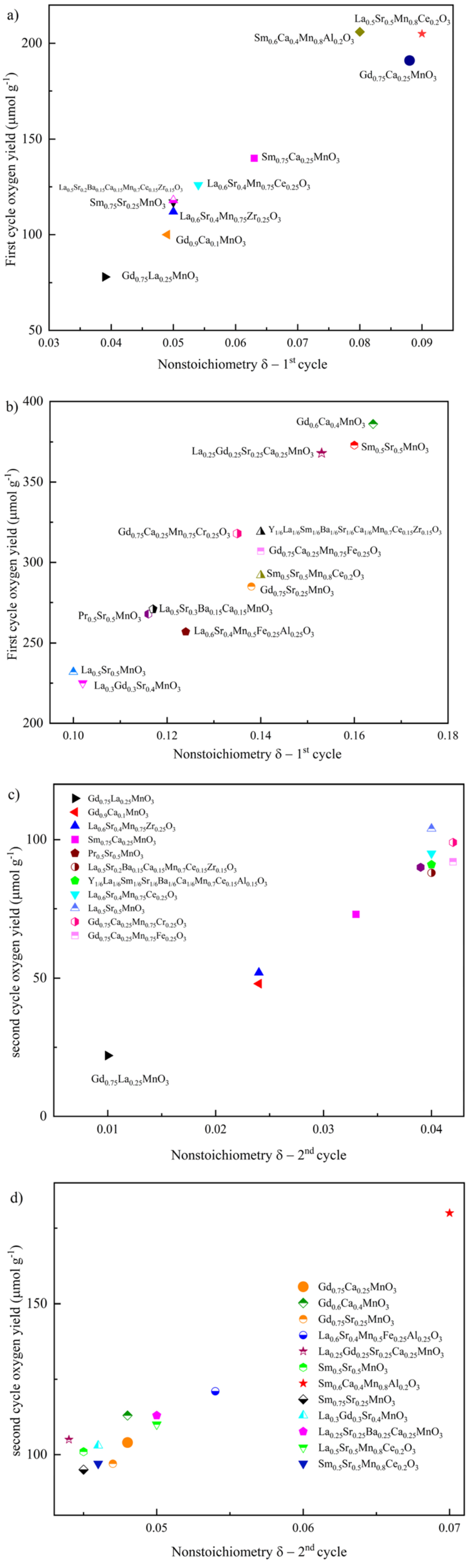

Fig. 5 Oxygen production yields of perovskites in two successive cycles: (a and b) first cycle for perovskites with low and high reduction extents, and (c and d) second cycle for perovskites with low and high reduction extents.

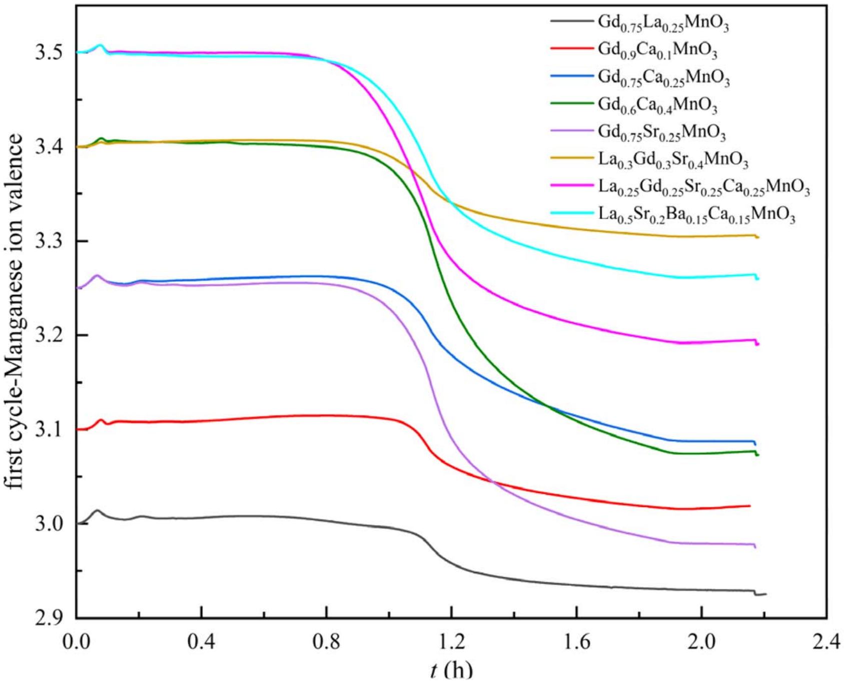

Fig. 6 Mn ion valence variation of A-site doped Mn-based perovskites for the reduction step of the first cycle.

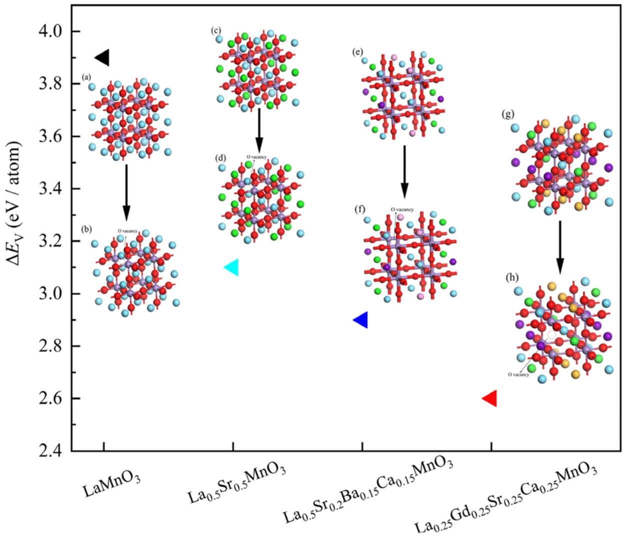

Fig. 7 Oxygen vacancy formation energy of the perovskites and variations with doping cations: (a) $LaMnO_3$, (b) oxygen deficient $LaMnO_3$, (c) $La_{0.5}Sr_{0.5}MnO_3$, (d) oxygen deficient $La_{0.5}Sr_{0.5}MnO_3$, (e) $La_{0.5}Sr_{0.2}Ba_{0.15}Ca_{0.15}MnO_3$, (f) oxygen deficient $La_{0.5}Sr_{0.2}Ba_{0.15}Ca_{0.15}MnO_3$, (g) $La_{0.25}Gd_{0.25}Sr_{0.25}Ca_{0.25}MnO_3$, and (h) oxygen deficient $La_{0.25}Gd_{0.25}Sr_{0.25}Ca_{0.25}MnO_3$. Blue atoms represent La, light purple atoms represent Mn, red atoms represent O, green atoms represent Sr, pink atoms represent Ba, deep purple atoms represent Ca, and yellow atoms represent Gd.

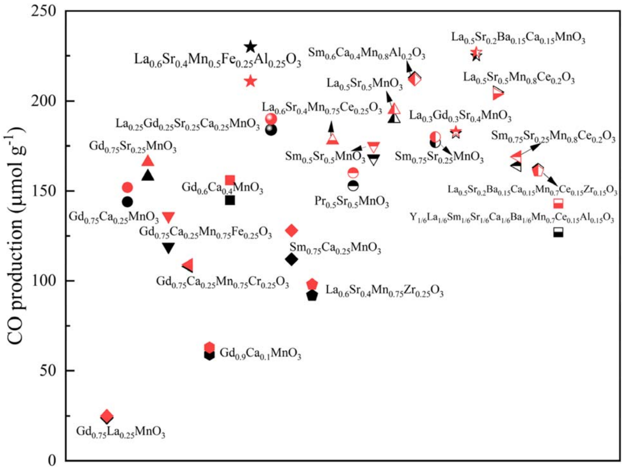

Fig. 8 CO production yields of 23 single, double, and multiple cation doped perovskites (black symbols represent the results of the first cycle and red symbols represent the results of the second cycle).

should be above 2.5 eV per (O atom) to overcome the energy barrier for the oxidation step. From the calculation results of the established CASTEP program, doping of the divalent cation Sr^{2+} causes an obvious decrease of the required energy for oxygen vacancy formation. Indeed, the oxygen vacancy formation energy decreases from 3.897 eV per (O atom) to 3.07 eV per (O atom). With the presence of multi-doping cations (Sr^{2+}, Ba^{2+}, and Ca^{2+}) in the A site, the reduction energy band further decreases to 2.91 eV per (O atom) for oxygen transfer. Although the global proportion of divalent cation doping is the same, the existence of multi-doping cations can reduce the energy barrier for oxygen transfer. In addition, the incorporation of Gd^{3+} leads to a further decrease in the oxygen vacancy formation energy to 2.57 eV per (O atom). The A-site high cation doping thus results in a significant decrease in the energy barriers for oxygen transfer, which supports the experimentally measured oxygen yield results.

3.2.2 CO production performance. The CO yields of the synthesized 23 perovskites are presented in Fig. 8. The black symbols represent the CO production results of the first cycle

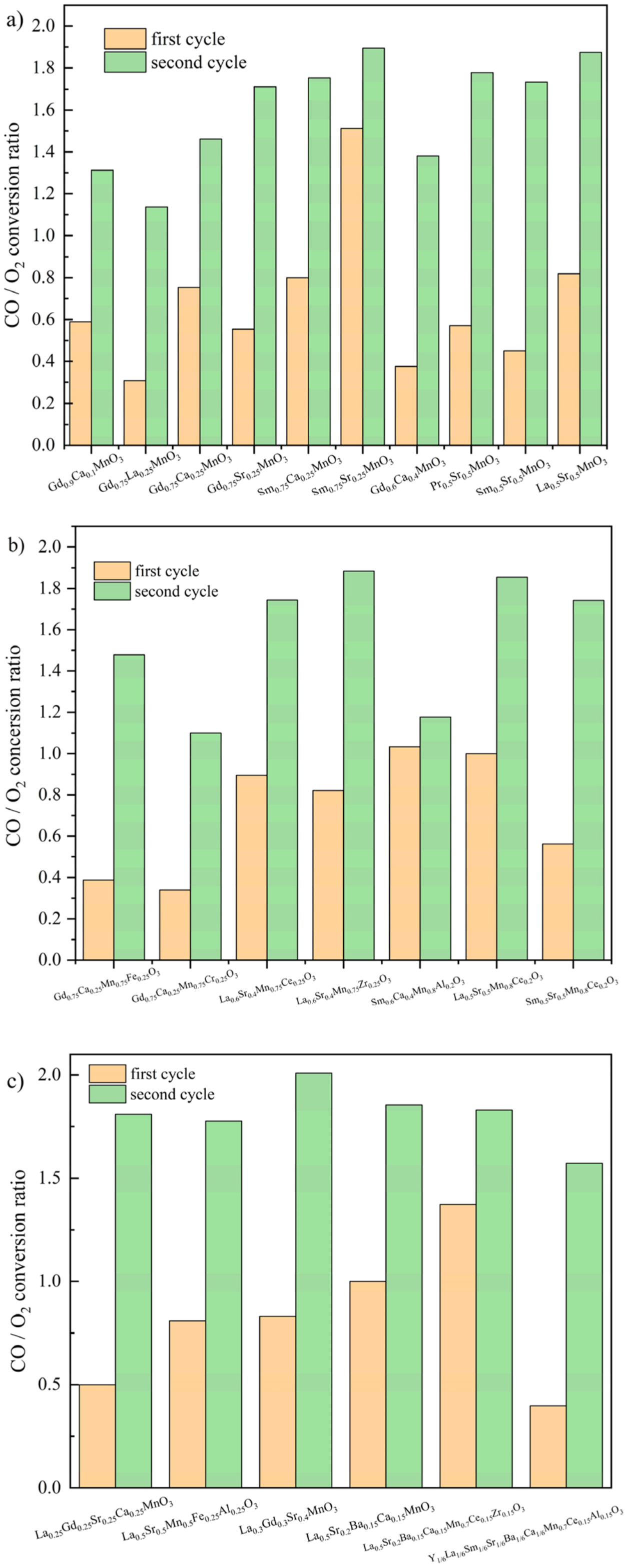

Fig. 9 CO/O_2 conversion ratios of (a) single doping, (b) double doping, and (c) multi doping of perovskites during two consecutive thermochemical cycles.

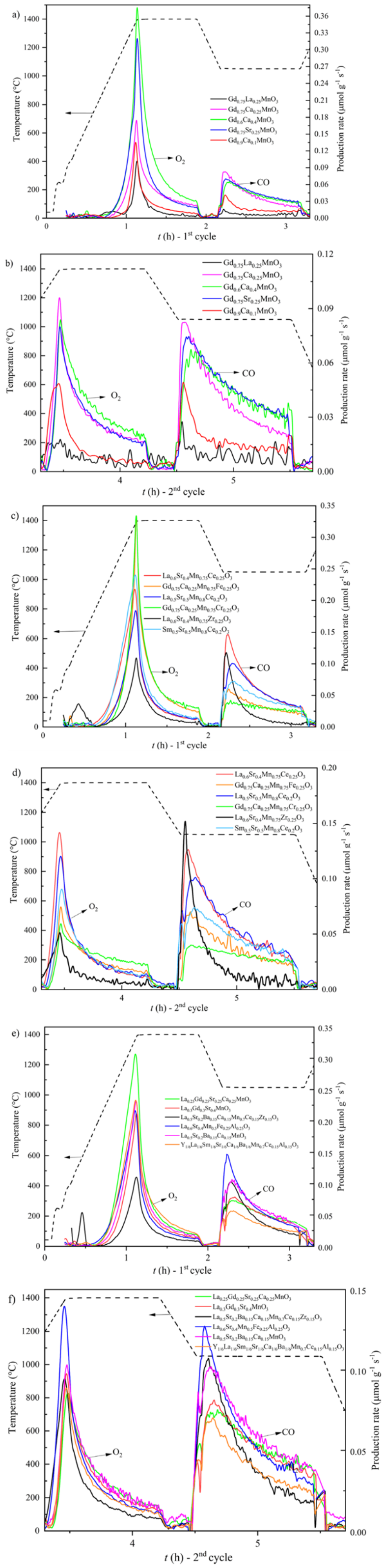

Fig. 10 Dynamic evolution of gas production rates of (a and b) single doping, (c and d) double doping, and (e and f) multi doping of perovskites in two consecutive cycles.

and the red symbols represent the CO yields of the second cycle. $La_{0.5}Sr_{0.2}Ba_{0.15}Ca_{0.15}MnO_3$ exhibits the best CO production performance in two consecutive thermochemical cycles, with the CO yields of 225 and 227 μmol g^{-1} respectively. Under the same thermochemical cycling conditions of this study, ceria is able to produce up to about 100 μmol_{CO} g^{-1} after a reduction step at 1400 °C and oxidation with 50% CO_2/Ar at 1050 °C.[37,54] The highest CO yield is obtained by $La_{0.6}Sr_{0.4}Mn_{0.5}Fe_{0.25}Al_{0.25}O_3$ (230 μmol g^{-1}), but the CO yield decreases slightly to 211 μmol g^{-1} in the second cycle. All of the synthesized perovskites show overall good stability, as evidenced by the CO production performance remaining stable in multiple cycles. Regarding the single cation doped perovskites, the presence of the Sr^{2+} cation results in higher CO yields than with the Ca^{2+} doped perovskites, and the most favorable single cation doped perovskite for CO_2 splitting is $La_{0.5}Sr_{0.5}MnO_3$. To improve the CO production performance, a strategy is to incorporate B site cations into the single cation doped perovskites. The doping of Al^{3+} and Ce^{3+} in the B site enhances CO production performance, whereas the doping of Fe^{3+}, Zr^{3+} and Cr^{3+} in the B site does not improve the CO yields. The Ce^{3+} incorporation into $La_{0.5}Sr_{0.5}MnO_3$ shows an obvious increase in the CO yield. On the basis of the individual A/B site cation doping effects, the multiple cation doped perovskites are designed with the aim to increase CO yields. Accordingly, two high-performance $La_{0.6}Sr_{0.4}Mn_{0.5}Fe_{0.25}Al_{0.25}O_3$ and $La_{0.5}Sr_{0.2}Ba_{0.15}Ca_{0.15}MnO_3$ perovskites are identified in this work. In contrast, the other considered high doping cations in both A and B sites do not show competitive CO yields.

3.2.3 CO/O_2 molar ratio. The CO/O_2 ratios achieved from redox cycling of synthesized perovskites are presented in Fig. 9. It compares the CO/O_2 ratio for each group of materials, which allows identification of the materials showing the highest conversion ratios among the considered formulations because this ratio is an important indicator of the reaction extent. The complete redox reactions lead to a conversion ratio of 2. It is observed that the CO/O_2 conversion ratio of all the materials exhibits an obvious increase in the second cycle. This is because the oxygen vacancies generated in the first cycle are not refilled completely, which benefits the CO_2 splitting in the second cycle. Regarding the single cation doped perovskites, $Sm_{0.75}Sr_{0.25}MnO_3$ shows the best CO/O_2 conversion performance, with the maximum conversion ratios of 1.51 and 1.89, respectively, while $Gd_{0.75}La_{0.25}MnO_3$ shows the lowest conversion ratio. The single cation doped perovskites with the incorporation of Sr^{2+} exhibit better CO/O_2 conversion than those with Ca^{2+} and La^{3+}. For the double cation doped perovskites, $Sm_{0.6}Ca_{0.4}Mn_{0.8}Al_{0.2}O_3$ has the highest CO/O_2 conversion ratio in the first cycle, although the ratio of the second cycle is low. In addition, the Fe^{3+} and Ce^{3+} doped perovskites show a good CO/O_2 conversion ratio in the second cycle. $Gd_{0.75}Ca_{0.25}Mn_{0.75}Cr_{0.25}O_3$ has the lowest conversion ratio compared with other double cation doped perovskites. It is noted that the CO/O_2 conversion ratios of all the high cation doped perovskites are over 1.5 in the second cycle.

3.3 Gas production rate analysis

The reaction kinetics for both cycle steps of the synthesized perovskites is essential for improving the process efficiency. The

Table 3 Peak reaction rates of perovskites in two consecutive cycles

	Peak O_2 production rates (μmol g^{-1} s^{-1})		Peak CO production rates (μmol g^{-1} s^{-1})	
	1st cycle	2nd cycle	1st cycle	2nd cycle
$Gd_{0.75}La_{0.25}MnO_3$	0.1	0.02	0.01	0.03
$Gd_{0.75}Ca_{0.25}MnO_3$	0.17	0.1	0.08	0.08
$Gd_{0.75}Sr_{0.25}MnO_3$	0.32	0.08	0.07	0.07
$Gd_{0.9}Ca_{0.1}MnO_3$	0.13	0.05	0.04	0.05
$Gd_{0.6}Ca_{0.4}MnO_3$	0.37	0.08	0.06	0.07
$Gd_{0.75}Ca_{0.25}Mn_{0.75}Fe_{0.25}O_3$	0.33	0.07	0.06	0.07
$Gd_{0.75}Ca_{0.25}Mn_{0.75}Cr_{0.25}O_3$	0.33	0.06	0.04	0.04
$La_{0.5}Sr_{0.5}MnO_3$	0.203	0.103	0.096	0.1
$La_{0.6}Sr_{0.4}Mn_{0.75}Zr_{0.25}O_3$	0.11	0.05	0.11	0.15
$La_{0.6}Sr_{0.4}Mn_{0.75}Ce_{0.25}O_3$	0.1	0.09	0.11	0.11
$La_{0.5}Sr_{0.5}Mn_{0.8}Ce_{0.2}O_3$	0.18	0.12	0.1	0.1
$Pr_{0.5}Sr_{0.5}MnO_3$	0.217	0.07	0.06	0.068
$Sm_{0.75}Ca_{0.25}MnO_3$	0.111	0.095	0.061	0.113
$Sm_{0.75}Ca_{0.25}Mn_{0.8}Al_{0.2}O_3$	0.278	0.406	0.231	0.096
$Sm_{0.5}Sr_{0.5}MnO_3$	0.29	0.08	0.068	0.074
$Sm_{0.5}Sr_{0.5}Mn_{0.8}Ce_{0.2}O_3$	0.24	0.09	0.07	0.07
$Sm_{0.75}Sr_{0.25}MnO_3$	0.148	0.14	0.097	0.136
$La_{0.3}Gd_{0.3}Sr_{0.4}MnO_3$	0.21	0.1	0.08	0.08
$La_{0.6}Sr_{0.4}Mn_{0.5}Fe_{0.25}Al_{0.25}O_3$	0.2	0.14	0.14	0.13
$La_{0.25}Gd_{0.25}Sr_{0.25}Ca_{0.25}MnO_3$	0.31	0.08	0.07	0.07
$La_{0.5}Sr_{0.2}Ba_{0.15}Ca_{0.15}MnO_3$	0.23	0.1	0.1	0.1
$La_{0.5}Sr_{0.2}Ba_{0.15}Ca_{0.15}Mn_{0.7}Ce_{0.15}Al_{0.15}O_3$	0.11	0.09	0.1	0.11
$Y_{1/6}La_{1/6}Sm_{1/6}Sr_{1/6}Ba_{1/6}Ca_{1/6}Mn_{0.7}Ce_{0.15}Al_{0.15}O_3$	0.23	0.09	0.05	0.07

results of the gas production rate calculation are presented in Fig. 10, and the peak reaction rates are shown in Table 3. All the materials are divided into three groups based on the doping strategies. Overall, $Gd_{0.6}Ca_{0.4}MnO_3$ shows the most rapid oxygen production rate in the first cycle, reaching a maximum value of 0.375 μmol g^{-1} s^{-1}, and $La_{0.6}Sr_{0.4}Mn_{0.5}Fe_{0.25}Al_{0.25}O_3$ has the highest oxygen production rate of 0.14 μmol g^{-1} s^{-1} in the second reduction step. It is found that the oxygen production rates are improved with the existence of active B-site doping cations such as Ce^{3+}, Fe^{3+}, and Al^{3+}. Compared with the single cation doped perovskites, the double doping and high doping of perovskites present better CO production rate performance in two consecutive cycles. The presence of Zr^{4+} allows for rapid CO production, but the CO rates decrease more rapidly in the oxidation step. The rate evolution tendency indicates that the promising perovskites should have both a high maximum CO production rate along with sustained high CO rates during the oxidation process. The A-site high doping of $La_{0.5}Sr_{0.2}Ba_{0.15}Ca_{0.15}MnO_3$ perovskite shows sustainable high CO production rates in two successive redox cycles, indicating high CO yields, but the maximum CO production rate is lower than the B-site doped $La_{0.6}Sr_{0.4}Mn_{0.75}Zr_{0.25}O_3$ and $La_{0.6}Sr_{0.4}Mn_{0.75}Ce_{0.25}O_3$ perovskites. The Ce^{3+} incorporated perovskites, such as $La_{0.6}Sr_{0.4}Mn_{0.75}Ce_{0.25}O_3$ and $La_{0.5}Sr_{0.5}Mn_{0.8}Ce_{0.2}O_3$, present high maximum CO production rates and sustainable high CO rates. In addition, the Fe^{3+} and Al^{3+} doped $La_{0.6}Sr_{0.4}Mn_{0.5}Fe_{0.25}Al_{0.25}O_3$ shows excellent CO production kinetics in two cycles. The results suggest that the selection of active B site cations is important to increase the maximum CO production rate, and some perovskites with A site high doping show sustainable high CO production rates in multiple cycles.

4 Conclusion

In summary, the fuel production performance of 23 potential perovskites was investigated in this work through both thermodynamic (DFT) and experimental TGA analyses. The incorporation of various cations into the perovskites was considered to improve gas production yields. The single cation doped, double cation doped, and multiple cation doped perovskites were synthesized by the Pechini sol–gel method and characterized by X-ray diffraction. All of the A-site doped perovskites remained in the form of a pure phase after the reactions, while the formulations with B-site cation incorporation, such as in $La_{0.5}Sr_{0.5}Mn_{0.8}Ce_{0.2}O_3$, may generate side products. The high proportion of divalent cations enhanced the oxygen transfer and the Gd^{3+} containing perovskite $Gd_{0.6}Ca_{0.4}MnO_3$ had an excellent oxygen yield of 386 μmol g^{-1}. According to the DFT calculation results, the A-site high doping of $La_{0.5}Sr_{0.2}Ba_{0.15}Ca_{0.15}MnO_3$ and $La_{0.25}Gd_{0.25}Sr_{0.25}Ca_{0.25}MnO_3$ showed a lower energy barrier for oxygen transfer than $La_{0.5}Sr_{0.5}MnO_3$, with the oxygen vacancy formation energy decreasing from 3.07 eV per (O atom) (for $La_{0.5}Sr_{0.5}MnO_3$) to 2.91 eV per (O atom) and 2.57 eV per (O atom), respectively. The most favorable perovskite for CO production is $La_{0.5}Sr_{0.2}Ba_{0.15}Ca_{0.15}MnO_3$, with CO yields of 225 and 227 μmol g^{-1} in two consecutive cycles, indicating that the high cation doping perovskites have the capacity to achieve significant fuel production. It is noted that the CO/O_2 conversion ratios of all the high doping perovskites are over 1.5 in the second cycle. The kinetic analysis reveals that the selection of active B site cations is important to increase the maximum CO production rate, and A site high doping perovskites sustained high CO production rates during the CO_2 dissociation process. This work focused on the A and/or B site cation doping effects on the fuel production capacity of different perovskites. Future work should focus on the stability during multiple cycles and fuel yield optimization of these perovskites.

Data availability

The data presented in this study are available in this article.

Conflicts of interest

The authors declare that they have no known competing financial interests or personal relationships that could have appeared to influence the work reported in this paper.

Acknowledgements

The one-year research stay of J. Cong at CNRS-PROMES was supported by the Chinese Academy of Sciences. The authors acknowledge the materials characterization platform of PROMES for providing the XRD analysis equipment.

References

1 R. J. Carrillo and J. R. Scheffe, Advances and Trends in Redox Materials for Solar Thermochemical Fuel Production, *Sol. Energy*, 2017, **156**, 3–20, DOI: **10.1016/j.solener.2017.05.032**.

2 D. Marxer, P. Furler, M. Takacs and A. Steinfeld, Solar Thermochemical Splitting of CO_2 into Separate Streams of CO and O_2 with High Selectivity, Stability, Conversion, and Efficiency, *Energy Environ. Sci.*, 2017, **10**, 1142–1149, DOI: **10.1039/c6ee03776c**.

3 M. Romero and A. Steinfeld, Concentrating Solar Thermal Power and Thermochemical Fuels, *Energy Environ. Sci.*, 2012, **5**, 9234–9245, DOI: **10.1039/c2ee21275g**.

4 A. Le Gal, M. Drobek, A. Julbe and S. Abanades, Improving solar fuel production performance from H_2O and CO_2 thermochemical dissociation using custom-made reticulated porous ceria, *Mater. Today Sustain.*, 2023, **24**, 100542, DOI: **10.1016/j.mtsust.2023.100542**.

5 A. Haeussler, S. Abanades, A. Julbe, J. Jouannaux, M. Drobek, A. Ayral and B. Cartoixa, Remarkable Performance of Microstructured Ceria Foams for Thermochemical Splitting of H_2O and CO_2 in a Novel High–Temperature Solar Reactor, *Chem. Eng. Res. Des.*, 2020, **156**, 311–323, DOI: **10.1016/j.cherd.2020.02.008**.

6 S. Zoller, E. Koepf, D. Nizamian, M. Stephan, A. Patané, P. Haueter, M. Romero, J. González-Aguilar, D. Lieftink, E. de Wit, *et al.*, A Solar Tower Fuel Plant for the

Thermochemical Production of Kerosene from H_2O and CO_2, *Joule*, 2022, **6**, 1606–1616.

7 B. Bulfin, J. Vieten, C. Agrafiotis, M. Roeb and C. Sattler, Applications and Limitations of Two Step Metal Oxide Thermochemical Redox Cycles; A Review, *J. Mater. Chem. A*, 2017, **5**, 18951–18966.

8 S. Abanades, Redox Cycles. Active Materials, and Reactors Applied to Water and Carbon Dioxide Splitting for Solar Thermochemical Fuel Production: A Review, *Energies*, 2022, **15**, 7061, DOI: **10.3390/en15197061**.

9 S. Abanades, A Review of Oxygen Carrier Materials and Related Thermochemical Redox Processes for Concentrating Solar Thermal Applications, *Materials*, 2023, **16**, 3582, DOI: **10.3390/ma16093582**.

10 C. L. Muhich, S. Blaser, M. C. Hoes and A. Steinfeld, Comparing the Solar-to-Fuel Energy Conversion Efficiency of Ceria and Perovskite Based Thermochemical Redox Cycles for Splitting H_2O and CO_2, *Int. J. Hydrogen Energy*, 2018, **43**, 18814–18831, DOI: **10.1016/j.ijhydene.2018.08.137**.

11 A. Haeussler, S. Abanades, J. Jouannaux, M. Drobek, A. Ayral and A. Julbe, Recent Progress on Ceria Doping and Shaping Strategies for Solar Thermochemical Water and CO_2 Splitting Cycles, *AIMS Mater. Sci.*, 2019, **6**, 657–684, DOI: **10.3934/MATERSCI.2019.5.657**.

12 R. R. Bhosale, G. Takalkar, P. Sutar, A. Kumar, F. AlMomani and M. Khraisheh, A Decade of Ceria Based Solar Thermochemical H2O/CO2 Splitting Cycle, *Int. J. Hydrogen Energy*, 2019, **44**, 34–60, DOI: **10.1016/j.ijhydene.2018.04.080**.

13 M. Kubicek, A. H. Bork and J. L. M. Rupp, Perovskite Oxides-a Review on a Versatile Material Class for Solar-to-Fuel Conversion Processes, *J. Mater. Chem. A*, 2017, **5**, 11983–12000.

14 A. A. Emery, J. E. Saal, S. Kirklin, V. I. Hegde and C. Wolverton, High-Throughput Computational Screening of Perovskites for Thermochemical Water Splitting Applications, *Chem. Mater.*, 2016, **28**, 5621–5634, DOI: **10.1021/acs.chemmater.6b01182**.

15 M. Ezbiri, M. Takacs, D. Theiler, R. Michalsky and A. Steinfeld, Tunable Thermodynamic Activity of LaxSr1−xMnyAl1−yO3−δ (0 ≤ x ≤ 1, 0 ≤ y ≤ 1) Perovskites for Solar Thermochemical Fuel Synthesis, *J. Mater. Chem. A*, 2017, **5**, 4172–4182, DOI: **10.1039/c6ta06644e**.

16 N. Gokon, K. Hara, Y. Sugiyama, S. Bellan, T. Kodama and C. Hyun-seok, Thermochemical TwoStep Water Splitting Cycle Using Perovskite Oxides Based on LaSrMnO3 Redox System for Solar H2 Production, *Thermochim. Acta*, 2019, **680**, 178374, DOI: **10.1016/j.tca.2019.178374**.

17 L. Wang, M. Al-Mamun, Y. L. Zhong, L. Jiang, P. Liu, Y. Wang, H. G. Yang and H. Zhao, Ca^{2+} and Ga^{3+} Doped $LaMnO_3$ Perovskite as a Highly Efficient and Stable Catalyst for Two-Step Thermochemical Water Splitting, *Sustainable Energy Fuels*, 2017, **1**, 1013–1017.

18 A. Haeussler, S. Abanades, J. Jouannaux and A. Julbe, Non-Stoichiometric Redox Active Perovskite Materials for Solar Thermochemical Fuel Production: A Review, *Catalysts*, 2018, **8**, 611, DOI: **10.3390/catal8120611**.

19 C. K. Yang, Y. Yamazaki, A. Aydin and S. M. Haile, Thermodynamic and Kinetic Assessments of Strontium-Doped Lanthanum Manganite Perovskites for Two-Step Thermochemical Water Splitting, *J. Mater. Chem. A*, 2014, **2**, 13612–13623, DOI: **10.1039/c4ta02694b**.

20 A. J. Carrillo, A. H. Bork, T. Moser, E. Sediva, Z. D. Hood and J. L. M. Rupp, Modifying La0.6Sr0.4MnO3 Perovskites with Cr Incorporation for Fast Isothermal CO2-Splitting Kinetics in 30 Solar-Driven Thermochemical Cycles, *Adv. Energy Mater.*, 2019, **9**, 1803886.

21 A. H. Bork, E. Povoden-Karadeniz and J. L. M. Rupp, Modeling Thermochemical Solar-to-Fuel Conversion: CALPHAD for Thermodynamic Assessment Studies of Perovskites, Exemplified for (La,Sr)MnO3, *Adv. Energy Mater.*, 2016, **7**, 1601086, DOI: **10.1002/aenm.201601086**.

22 A. Haeussler, A. Julbe and S. Abanades, Investigation of Reactive Perovskite Materials for Solar Fuel Production via Two-Step Redox Cycles: Thermochemical Activity, Thermodynamic Properties and Reduction Kinetics, *Mater. Chem. Phys.*, 2022, **276**, 125358, DOI: **10.1016/j.matchemphys.2021.125358**.

23 A. Le Gal, A. Julbe and S. Abanades, Thermochemical Activity of Single- and Dual-Phase Oxide Compounds Based on Ceria, Ferrites, and Perovskites for Two-Step Synthetic Fuel Production, *Molecules*, 2023, **28**, 4327, DOI: **10.3390/molecules28114327**.

24 M. M. Nair and S. Abanades, Cation Synergy in Sr and Al Substituted LaMnO3 during Solar Thermochemical CO2 Splitting, *Energy Adv.*, 2023, **2**, 137–147, DOI: **10.1039/D2YA00309K**.

25 M. M. Nair and S. Abanades, Insights into the Redox Performance of Non-Stoichiometric Lanthanum Manganite Perovskites for Solar Thermochemical CO_2 Splitting, *ChemistrySelect*, 2016, **1**, 4449–4457, DOI: **10.1002/slct.201601171**.

26 M. M. Nair and S. Abanades, Experimental Screening of Perovskite Oxides as Efficient Redox Materials for Solar Thermochemical CO_2 Conversion, *Sustainable Energy Fuels*, 2018, **2**, 843–854, DOI: **10.1039/C7SE00516D**.

27 J. M. Naik, C. Ritter, B. Bulfin, A. Steinfeld, R. Erni and G. R. Patzke, Reversible Phase Transformations in Novel Ce-Substituted Perovskite Oxide Composites for Solar Thermochemical Redox Splitting of CO_2, *Adv. Energy Mater.*, 2021, **11**, 2003532.

28 D. R. Barcellos, M. Sanders, J. Tong, A. H. McDaniel and R. O'Hayre, BaCe0.25Mn0.75O3-δ - A Promising Perovskite-Type Oxide for Solar Thermochemical Hydrogen Production, *Energy Environ. Sci.*, 2018, **11**, 3256–3265, DOI: **10.1039/c8ee01989d**.

29 A. H. McDaniel, E. C. Miller, D. Arifin, A. Ambrosini, E. N. Coker, R. O'Hayre, W. C. Chueh and J. Tong, Sr- and Mn-Doped LaAlO3-δ for Solar Thermochemical H2 and CO Production, *Energy Environ. Sci.*, 2013, **6**, 2424–2428, DOI: **10.1039/c3ee41372a**.

30 C. Liu, J. Park, H. A. De Santiago, B. Xu, W. Li, D. Zhang, L. Zhou, Y. Qi, J. Luo and X. Liu, Perovskite Oxide Materials for Solar Thermochemical Hydrogen Production from Water Splitting through Chemical Looping, *ACS Catal.*, 2024, **14**, 14974–15013.

31 G. Sai Gautam, E. B. Stechel and E. A. Carter, Exploring Ca-Ce-M-O (M = 3d Transition Metal) Oxide Perovskites for Solar Thermochemical Applications, *Chem. Mater.*, 2020, **32**, 9964–9982.

32 S. S. Naghavi, J. He and C. Wolverton, $CeTi_2O_6$ - A Promising Oxide for Solar Thermochemical Hydrogen Production, *ACS Appl. Mater. Interfaces*, 2020, **12**, 21521–21527.

33 A. Bayon, A. de la Calle, K. K. Ghose, A. Page and R. McNaughton, Experimental, Computational and Thermodynamic Studies in Perovskites Metal Oxides for Thermochemical Fuel Production: A Review, *Int. J. Hydrogen Energy*, 2020, **45**, 12653–12679, DOI: 10.1016/j.ijhydene.2020.02.126.

34 C. Liu, D. Zhang, W. Li, J. Trindell, K. A. King and R. Sean, Bishop Manganese-Based A-Site High-Entropy Perovskite Oxide for Solar Thermochemical Hydrogen Production, *J. Mater. Chem. A*, 2024, **12**, 3910–3922.

35 Q. Wang, Y. Xuan, K. Gao, C. Sun, Y. Gao, J. Liu, S. Chang and X. Liu, High-Entropy Perovskite Oxides for Direct Solar-Driven Thermochemical CO2 Splitting, *Ceram. Int.*, 2024, **50**, 1564–1573, DOI: 10.1016/j.ceramint.2023.10.248.

36 A. Sarkar, Q. Wang, A. Schiele, M. R. Chellali, S. S. Bhattacharya, D. Wang, T. Brezesinski, H. Hahn, L. Velasco and B. Breitung, High-Entropy Oxides: Fundamental Aspects and Electrochemical Properties, *Adv. Mater.*, 2019, **31**, 1806236, DOI: 10.1002/adma.201806236.

37 A. Le Gal, S. Abanades and G. Flamant, CO2 and H2O Splitting for Thermochemical Production of Solar Fuels Using Nonstoichiometric Ceria and Ceria/Zirconia Solid Solutions, *Energy Fuels*, 2011, **25**, 4836–4845, DOI: 10.1021/ef200972r.31.

38 R. D. Barcellos, M. D. Sanders, J. Tong, A. H. McDaniel and R. P. O'Hayre, BaCe0.25Mn0.75O3-δ - Promising Perovskite-Type Oxide for Solar Thermochemical Hydrogen Production, *Energy Environ. Sci.*, 2018, **11**, 3256–3265, DOI: 10.1039/c8ee01989d.

39 J. Jouannaux, A. Haeussler, M. Drobek, A. Ayral, S. Abanades and A. Julbe, Lanthanum Manganite Perovskite Ceramic Powders for CO_2 Splitting: Influence of Pechini Synthesis Parameters on Sinterability and Reactivity, *Ceram. Int.*, 2019, **45**, 15636–15648, DOI: 10.1016/j.ceramint.2019.05.075.

40 M. Rini, R. Tobey, N. Dean, J. Itatani, Y. Tomioka, Y. Tokura, R. W. Schoenlein and A. Cavalleri, Control of the Electronic Phase of a Manganite by Mode-Selective Vibrational Excitation, *Nature*, 2007, **449**, 72–74, DOI: 10.1038/nature06119.

41 Z. Li, M. Yang, J. S. Park, S. H. Wei, J. J. Berry and K. Zhu, Stabilizing Perovskite Structures by Tuning Tolerance Factor: Formation of Formamidinium and Cesium Lead Iodide Solid-State Alloys, *Chem. Mater.*, 2016, **28**, 284–292.

42 S. A. Heuer, R. Schierholz, E. V. Alekseev, L. Peters, D. N. Mueller, T. Duchoň, V. Vibhu, H. Tempel, L. G. J. De Haart, H. Kungl, *et al.*, Oxygen Nonstoichiometry and Valence State of Manganese in La1-XCaxMnO3+δ, *ACS Omega*, 2021, **6**, 9638–9652.

43 R. D. Shannon, Revised Effective Ionic Radii and Systematic Studies of Interatomie Distances in Halides and Chaleogenides, *Acta Crystallogr., Sect. A*, 1976, **32**, 751–767.

44 T. Maiti, R. Banerjee, S. Chatterjee, M. Ranjan, T. Bhattacharya, S. Mukherjee, S. S. Jana and A. Dwivedi, High-Entropy Perovskites: An Emergent Class of Oxide Thermoelectrics with Ultralow Thermal Conductivity, *ACS Sustain. Chem. Eng.*, 2020, **8**, 17022–17032.

45 J. Vieten, B. Bulfin, P. Huck, M. Horton, D. Guban, L. Zhu, Y. Lu, K. A. Persson, M. Roeb and C. Sattler, Materials Design of Perovskite Solid Solutions for Thermochemical Applications, *Energy Environ. Sci.*, 2019, **12**, 1369–1384, DOI: 10.1039/c9ee00085b.

46 S. Ašmontas and M. Mujahid, Recent Progress in Perovskite Tandem Solar Cells, *Nanomaterials*, 2023, **13**, 1886, DOI: 10.3390/nano13121886.

47 S. A. Hassanzadeh-Tabrizi, Precise Calculation of Crystallite Size of Nanomaterials: A Review, *J. Alloys Compd.*, 2023, **968**, 171914.

48 R. J. Panlener, R. N. Blumenthal and J. E. Garnier Medley, A Thermodynamic study of nonstoichiometric cerium dioxide, *J. Phys. Chem. Solids*, 1975, **36**, 1213–1222.

49 V. Milman, B. Winkler, J. A. White, C. J. Pickard, M. C. Payne, E. V. Akhmatskaya and R. H. Nobes, Electronic Structure, Properties, and Phase Stability of Inorganic Crystals: A Pseudopotential Plane-Wave Study, *Int. J. Quantum Chem.*, 2000, **77**, 895–910.

50 C. C. Pan, Y. H. Chen, N. Wu, M. L. Zhang, L. H. Yuan and C. R. Zhang, First-Principle Study of O Vacancy on LaNiO3 (001) Surface, *Int. J. Hydrogen Energy*, 2016, **41**, 15756–15763, DOI: 10.1016/j.ijhydene.2016.04.143.

51 A. A. Emery, J. E. Saal, S. Kirklin, V. I. Hegde and C. Wolverton, High-Throughput Computational Screening of Perovskites for Thermochemical Water Splitting Applications, *Chem. Mater.*, 2016, **28**, 5621–5634, DOI: 10.1021/acs.chemmater.6b01182.

52 D. Vanderbilt, Soft Self-Consistent Pseudopotentials in a Generalized Eigenvalue Formalism, *Phys. Rev. B*, 1990, **41**, 7892–7895.

53 J. P. Perdew, K. Burke and M. Ernzerhof, Generalized Gradient Approximation Made Simple, *Phys. Rev. Lett.*, 1996, **77**, 3865–3868.

54 S. Abanades, A. Haeussler and A. Julbe, Synthesis and Thermochemical Redox Cycling of Porous Ceria Microspheres for Renewable Fuels Production from Solar-Aided Water-Splitting and CO2 Utilization, *Appl. Phys. Lett.*, 2021, **119**, 023902, DOI: 10.1063/5.0055282.